International Union of Crystallography

Commission on Crystallographic Apparatus

Accuracy of Structure Factors from X-ray Powder Intensity Measurements*

By P. Suortti, *Department of Physics, University of Helsinki, Siltavuorenpenger 20 D, Helsinki 17, Finland* and L. D. Jennings, *Army Materials and Mechanics Research Center, Watertown, Mass. 02172, USA*

The accuracy of the determination of the structure factors from a powder diffraction measurement is studied in light of a representative example: nickel with Cu *K*α radiation. Various sources of error in the absolute measurement and methods of sample characterization are discussed. The contributions of various extraneous scattering mechanisms are assessed. From these considerations it is possible to separate the Bragg scattering, providing measurements are made through virtually the entire angular range. Results are given in detail for a standard sample, a duplicate of which can be made available to interested workers. The relationship of these results to the structure factors of the sample is discussed in terms of a model calculation, in terms of line shape analysis, and in terms of some comparative measurements on various samples of Ni and MgO. All these analyses indicate the impossibility of preparing a single sample which is ideally mosaic. Thus it is incorrect to relate the measured integrated reflection to the structure factor with the customary simple formula when high accuracy is required.

Introduction

There are many possible reasons for measuring the X-ray Bragg scattering from powders, but most of these do not require intensity values of the highest attainable accuracy. For some purposes though, such as the testing of physical theories of charge redistribution in solids, structure factors must be determined as accurately as possible. Clearly, in such cases, it is necessary to measure each structure factor on an absolute basis and on its own merits, without reference to theory to determine, for example, a scaling factor or an extinction correction. This paper discusses the current state of the art of making such structure factor determinations on the basis of intensity measurement of powdered samples.

The evaluation of the structure factors can perhaps be divided into two steps: the measurement of the elastically scattered intensity and the conversion of this intensity to structure factor values. Because it is not completely clear where to draw the line between these two steps and because of conflicting requirements on the sample preparation, we feel that it is important to discuss both these steps together. It is our thesis that it is possible to determine the elastically scattered intensity with an absolute accuracy of better than $\frac{1}{2}\%$ for a suitably prepared sample. We discuss many of the corrections which are necessary to convert these intensities to structure factors, but we show that present-day methods are scarcely adequate to obtain structure factors with comparable accuracy. To verify our statement about experimental accuracy and to elucidate the structure factor situation, we wish to encourage international cooperation. To this end, we are making available well characterized samples of carbonyl process nickel powder, and a major portion of this paper is a description of the experiments and calculations we thought were necessary for a satisfactory characterization. Other workers can then compare their own results with ours with help of this standard sample. Duplicates of these

standard samples are available to interested workers from one of the authors (P.S.).

The above point of view has developed as a consequence of the Powder Intensity Project (1966–69) sponsored by the Commission on Crystallographic Apparatus of the IUCr. The findings of this Project have been reported (Jennings, 1969; Miller & Black, 1970; Paakkari, Suortti & Inkinen, 1970; Linkoaho, Rantavuori & Korhonen, 1971) and can be summarized as follows:

– Participation was too limited (12 data sets from 10 laboratories) to allow a valid statistical analysis.

– The values of the integrated intensities measured from identical specimens were disappointingly widespread, by 5 to 10%, but the absolute values were no worse than the relative ones.

– Only three participants were able to furnish information on the scattering between Bragg reflections, and these sets showed much closer agreement.

Because of this latter result, we believe that a study of *all* the components of the scattering is necessary for the accurate measurement of Bragg scattering. For example, it is impossible to know the correct limits of a Bragg peak without knowing the shape of the thermal diffuse scattering (TDS).

Further advances in instrumentation and theory led the 1972–1975 Commission to believe that a new intensity measurement project would be useful in delineating the proper method for accurate intensity measurements. However, the results of a questionnaire sent to 45 laboratories resulted in a negative approach to a project involving the participation of several laboratories. This report is the result of a decision by the Commission to prepare a review article summarizing current knowledge of the best techniques available for measuring accurately intensities of powder samples, and for analyzing them.

In keeping with the objective of the paper, we give enough detail to yield an appreciation for each of the problems involved. We cannot give a complete treatment of each aspect, and references are made to more detailed reports. In § I.1 we discuss the diffraction apparatus. § I.2 deals with the preparation of the standard nickel samples, both from the point of

---

* Duplicates of the standard sample with test results, instructions and report format are available from P. Suortti on request. A modest fee will be charged for the standard samples.

view of intensity measurements and of some properties needed to determine structure factors: preferred orientation and porosity. § II.1 discusses separately those components of the background which undergo appreciable energy shift, and the TDS and Compton scattering, which are only slightly shifted. The evaluation of the Bragg intensities is then reported in § II.2. Finally, in § II.3, we discuss some aspects of the nature of the scattering process which cause additional problems in relating the Bragg intensities to true structure factors. We demonstrate the inadequacy of the current kinematical theory of X-ray diffraction in this sense and therefore we limit the discussion to considerations relevant to the experimental procedure. Thus the physical significance of the results, as with respect to the charge distribution, is not discussed.

I. EXPERIMENTAL

I.1. Diffraction geometry

1.1 *Geometrical aberrations*

The displacements and divergences of the incident and detected beams give rise to several deviations from the idealized geometry of very narrow beams. Their effects on the profiles of the diffraction maxima are pronounced, and these effects have been studied extensively (cf. Wilson, 1963). The changes in the integrated intensities and in the background are less obvious, but they have been treated by Suortti & Jennings (1971). Most of the practical cases in powder diffraction are covered, and the effects are not necessarily negligible. They are of three types:
– Beam penetration into the sample.
– Misalignment; the formulas of Suortti & Jennings (1971) give criteria for the alignment procedure; the essential requirement is that the axis of the goniometer contains the center of gravity of the incident beam and the surface of the sample.
– Divergences; reliable corrections allow for larger divergences, which can be desirable for the sake of increased intensity.

In the present case, intensity was no great problem and it was convenient to restrict the divergences. Furthermore, the use of a large, stationary receiving slit reduces the effects of geometrical aberrations on the received power in comparison with the usual $\theta-2\theta$ scan with a narrow slit. Thus the only appreciable effects were due to axial divergences: a 0.15% increase in the Bragg power in the two highest angle reflections, 331 and 420, and a nearly angularly independent lowering of the diffuse background by 0.2%.

1.2 *Elimination of the parasitic components*

Commercial diffractometers are not usually designed to make highly accurate intensity measurements possible and some reconstruction is often required. For example, although air and slit scatter can be measured separately and subtracted, it is much more convenient to eliminate them. This can be accomplished with beam tunnels and a vacuum chamber as shown in Fig. 1. Other details of practical importance are discussed by Chipman (1969) and Paakkari et al. (1970).

1.3 *Monochromator*

A true absolute measurement of the diffracted intensity is not feasible unless the detected radiation is approximately monochromatic. A bent-crystal monochromator may be placed in the diffracted beam or in the primary beam, as shown in Fig. 1. The operation of the monochromator

depends not only on the characteristics of the crystal, but also on the geometrical arrangement and the spectral content of the beam. These complications make it extremely difficult to avoid serious errors when the monochromator is in the diffracted beam (Paakkari et al., 1970; Linkoaho et al., 1971), even when an elastically bent quartz crystal is used. This result is true for relative measurements, but the difficulties are even greater for an absolute measurement, where both the direct and the diffracted beam must be measured, and they have different distributions. Thus we will consider only an incident-beam monochromator, in which case one may use plastically bent LiF or oriented graphite which are more efficient but less uniform than quartz. We will discuss these materials with respect to homogeneity, beam purity, and polarization ratio.

1.3.1 *Homogeneity*

Because of the mosaic nature of the crystal, imperfections in the bending process, imperfect alignment, etc., the monochromated beam is non-uniform. Because the powder sample is presumed to be homogeneous, this non-uniformity is not a critical shortcoming. It is necessary, however, to make suitable measurements of the power distribution in the beam to carry out the alignment and corrections discussed in § I.1.1.

1.3.2 *Beam purity and power*

In addition to the desired wavelength λ, the beam is contaminated by nearby wavelengths and harmonics which are Bragg reflected from the monochromator and also by remote wavelengths which are diffusely scattered. These contaminants may be studied by energy analysis of the beam as attenuated by appropriately chosen absorbers and also by measuring the angular dependence of Bragg diffraction in the usual spectrometer arrangement. We will restrict ourselves to a few illustrative remarks based on the Cu $K\alpha$ units used for the Ni and MgO experiments discussed here.
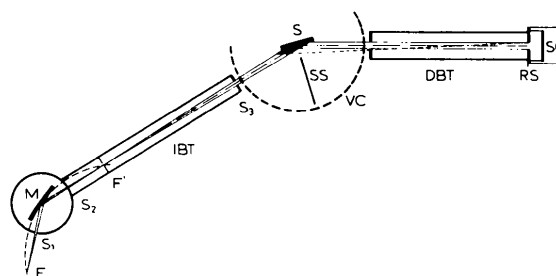

Fig. 1. Equatorial cross section of diffraction geometry. F is the line target of the X-ray tube, M the Johann type monochromator with housing, IBT the incident beam tunnel, S the sample, VC the vacuum chamber, and SS an additional shield which prevents scattering from the Be window entering the diffracted beam tunnel DBT. RS is the receiving slit and SC the scintillation counter. The distances are: $F - M = M - F' = 53$ mm, $F - S_1 = S_2 - F' = 33$ mm, and $F' - S_3 = 107$ mm. The radius of the goniometer, $F' - S = S - RS$, is 170 mm. The sizes of the slits were normally (equatorial × axial): $S_1 = S_2 = 1.0 \times 6.0$ mm, $S_3 = 0.8 \times 4.0$ mm, and the width of the focal slit at F' 0.3 mm. The slit sizes are not optimized for maximum intensity, and the sample of 20 mm diameter would allow larger slits. The shaded area in front of the sample indicates the scattering air volume that is seen by the receiving slit, if the vacuum chamber is not used.

The projected width of the focal line of the X-ray tube is typically 0·1 mm and the width of the focal slit F' may safely be chosen to be only somewhat larger. Under these conditions the wavelength band accepted is comparable to the $\alpha_1-\alpha_2$ separation. Therefore it is necessary to make a study to determine the average wavelength. However, the effect of the wavelength convolution can be estimated from the $\alpha_1-\alpha_2$ separation and is usually negligible, except in connection with attenuation of the main beam. The effect of diffuse scattering from the monochromator was also negligible as
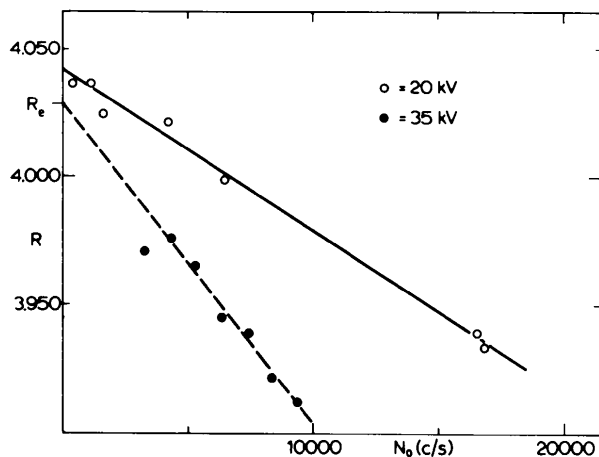

Fig. 2. Determination of the effective attenuation, R_e, of a Ni absorber with $\lambda/3$ and $\lambda/4$ components present in the primary beam (35 kV), and without these components (20 kV). R_e has dead time removed, but is influenced by the spectral distribution. N_0 is the count rate without the attenuator, and at 35 kV N_0 is varied by changing the tube current in order to retain the wavelength composition. The dead time is obtained from the figure: $\tau = \text{slope}/(1-R_e)$. In the present case $R_e = 4·042$, $\tau = 2·09$ μs for 20 kV, and $R_e = 4·028$, $\tau = 4·22$ μs for 35 kV.
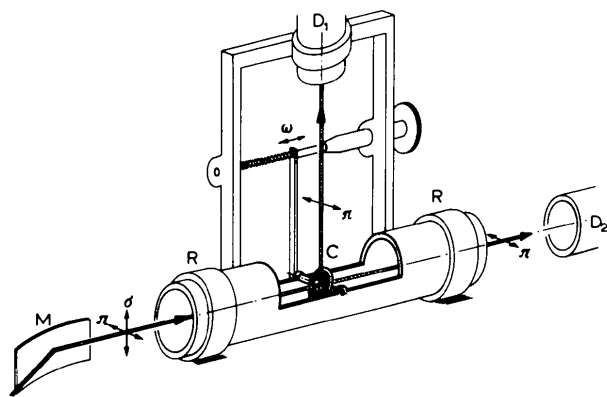

Fig. 3. Device for measurement of the polarization ratio, K; in the figure set for π polarization. The structures are attached to a hollow cylinder, supported by rings R so as to allow a 90° rotation to measure the σ polarization. The axis of the cylinder is aligned to coincide with the incident beam from monochromator M. C is a perfect crystal or a powder sample, and D_1 and D_2 are the detector positions in reflection and transmission, respectively. The ω scan is arranged with a micrometer screw driven by a synchronous motor; in the powder measurement the motor spins the specimen by chord transmission.

could be verified most easily by scanning for the Cu $K\beta$ wavelength.

The harmonic wavelengths make only a weak contribution to the Bragg reflections from the sample and may be adequately removed by a pulse-height analyser (PHA). They can, however, cause troublesome sample fluorescence, spurious minor peaks, or manifest themselves in other ways.

The power in the incident beam is measured after attenuation by a number of nearly identical foils of β-filter material (nickel in the present case). In our experience this method is far preferable to any other. The process of calibrating the foils also characterizes the counting apparatus. The situation is discussed in detail by Chipman (1969), but some points are illustrated by the following example. The open symbols in Fig. 2 show the determination of dead time and foil ratio for a beam which contains only a fraction of one percent $\lambda/2$ and no higher harmonics. The full symbols show a similar measurement on a beam which was so hardened by transmission through a series of Ni foils that it contained about 70% $\lambda/3$ plus $\lambda/4$. Although the PHA removes most of the counts from these harmonics, a few are accepted and the apparent absorption of the foil is reduced. Furthermore, all received photons disable the counting train and thus the effective dead time per Cu $K\alpha$ photon is markedly increased.

Such considerations suggest the following practice in an absolute measurement:

- The absolute scale is established for a strong reflection using an exciting voltage below the $\lambda/3$ or $\lambda/2$ limit as necessary.
- If greater beam power is required, relative measurements of Bragg peaks or the diffuse scattering may be made with a higher exciting voltage.

1.3.3 Polarization ratio

To interpret the scattering from the sample, it is necessary to know the polarization ratio K of the incident beam. This is defined as the ratio of the power polarized in the plane of diffraction (π) to the power polarized perpendicularly to this plane (σ). For a diffracted-beam monochromator, an analogous definition is possible. In any case, the value of K is a complicated function of the properties of the monochromating crystal, the geometry of the apparatus, and (perhaps) of the X-ray source. For the arrangement of Fig. 1, K lies between $\cos^2 2\theta_M$ and unity (not necessarily between $\cos^2 2\theta_M$ and $\cos 2\theta_M$ as has sometimes been stated), but it is not possible to calculate an accurate value. The fact that K may exceed the dynamical value is a result of large secondary extinction typical in good monochromator crystals (Zachariasen, 1945).

Rough values of K are easily obtained; we have measured air scattering at 90° with the counter first in the usual plane of diffraction and then placed so as to observe the other polarization. Values accurate to about 1% may be obtained in a short time in this way. But the overall experimental results are no more accurate than the polarization factor. Accuracies of 0·1% are obtained only with difficulty and are almost impossible for a diffracted-beam monochromator. The accurate methods for measuring K are illustrated in the device of Fig. 3, which replaces the sample in the arrangement of Fig. 1. Its modes are:

(a) A nearly 90° reflection from a perfect crystal (Ge 333 for Cu $K\alpha$ radiation) is scanned in the π and σ planes.

(b) The integrated intensity of nearly 90° powder reflection is measured in the π and σ planes with a stationary receiving slit.

(c) A perfect crystal is rocked through the anomalous transmission position in the π and σ planes.

In all cases, care and understanding are required, but K is given by the observed intensity ratio. In cases (a) and (b), small corrections are required for rays which do not diffract at the idealized angle. In case (b) an adequately uniform sample may usually be obtained by spinning the specimen. The different beam divergences and focusing conditions in the π and σ planes give rise to complications in all cases. In case (c) there may be spectral impurities in the transmitted beam. In cases (a) and (b) the included TDS may be appreciable, but it can be determined by an examination of the wings of the reflection measured with good collimation or focusing. It can then be taken into account through a convolution with the beam divergence. More detailed discussion may be found in papers by Jennings (1968), Suortti & Paakkari (1968), Olekhnovich (1969, 1970), Paakkari et al. (1970), and Linkoaho et al. (1971).

The importance of these considerations is indicated in Table 1, which gives some values of K under typical conditions, measured in connection with the present work. Values of $\cos 2\theta$ and $\cos^2 2\theta$ are given for reference. The polarization ratio clearly depends on whether the beam incident on the monochromator has a divergence which is large or small compared to the mosaic spread of the monochromator. The polarization ratio would be more nearly unity in the latter case.

Table 1. *Values of polarization ratio, K, for various conditions*

For any material, conditions may be changed by deforming the monochromating crystal or by altering the beam divergences; the equatorial divergence with respect to the mosaic spread of the monochromator crystal is indicated in the table. The bending radius is denoted by 2R.

Material	Beam divergence	$2R$ (mm)	$\cos 2\theta_M$	$\cos^2 2\theta_M$	K
Graphite	Small	230	0·894	0·800	0·925
(00.2)	Large	230			0·905
Quartz	Large	500	0·894	0·799	0·915
(10.1)	Large	250			0·905
LiF	Large	250	0·707	0·499	0·780
(200)	Large	200			0·730

1.4 Recording of intensity

1.4.1 Detector

A solid-state detector (SSD) would be preferable for recording the intensity, but one is still expensive and usually the detector crystal is too small. An SSD is indispensable in the energy analysis of the scattered radiation, which will be discussed later. In other respects, a scintillation counter can meet the requirements of an accurate diffraction measurement.

Methods for measuring dead time and spectral purity of the beam have already been mentioned in § 1.3.2. These questions and many other details of photon counting are discussed by Chipman (1969) and Paakkari et al. (1970). It should be reemphasized, however, that scintillation crystals often deteriorate rapidly, and the various checks should be frequently repeated.

1.4.2 Strategy of measurement

The best strategy of measurement depends on the available apparatus and the objective of the study. The measurements reported here were designed to meet the following requirements:

– All measurements are on an absolute basis.
– Information is easy to process with a computer.
– Statistical accuracy is optimized.
– Both the profiles and the integrals of the Bragg reflections are needed.

The background and the reflections were step-scanned, and the photon count was punched on paper tape. The step and the opening of the receiving slit were varied depending on the rate of change of the scattered intensity with angle. The power of the primary beam was measured at the beginning and end of each series of measurements.

The integrated intensities of the Bragg reflections were measured with a wide-open, stationary receiving slit. The following things favor this arrangement over the customary θ–2θ scan:

– The power of the detected beam is large, and so the order of 10^5 counts were accumulated in a short time even for the weakest reflections.
– The dead-time correction is convenient to apply.
– Only the height of the receiving slit must be known accurately.
– The shape of the slit edges is not critical.
– The effects of the geometrical aberrations are strongly reduced.

In practice, a standard receiving slit ($4\cdot0°$ in 2θ) was used for all reflections. The dimensions of this slit were measured by scanning it through a pin-hole beam at several places along the length and width. Relative areas of other slits were determined by comparing received powers in a fluorescence experiment. The detailed analysis of § II.1 was used to estimate the amount of Bragg scattering not included in the standard stationary slit measurement as well as the amount of non-Bragg scattering which was included.

I.2. Sample characterization

Insofar as the preparation of a standard sample is concerned, the only problems are those of reproducibility and homogeneity. For scattering factor measurements, however, it is necessary to take into account other considerations. Granularity and preferred orientation are conveniently studied using a single powder and these effects are discussed here. Primary extinction is best studied using a series of powders and is discussed in § II.3. In principle, secondary extinction is not a problem since, for an ideal powder, it only increases the absorption coefficient (DeMarco & Suortti, 1971).

2.1 Sample preparation

The most critical point in preparation of the sample is the selection or preparation of the powder. The absorption properties, i.e. the degree of porosity and surface roughness, are determined by the particle size and shape, and the grain size controls primary extinction. In principle a loosely packed specimen would fulfill the requirement of non-interacting, randomly oriented particles, but in practice a well defined, homogenous sample cannot be prepared without compression. The stress field changes the initial values of porosity, surface roughness and primary extinction, but also preferred orientation is introduced. Each of these phenomena should be followed independently, and the final selection of the sample should be made in the way that minimizes the overall uncertainty due to these aberrations.

We developed a sample preparation procedure which

would make the samples as identical as possible and would also preclude the most obvious sources of inhomogeneity. The powder was poured into the die through a coarse sieve (opening about 50 times the particle size), which dispersed the powder uniformly without any initial pressure. From this column of powder, the lowest portion in the sample holder was separated by a thin metal leaf. The filling device was removed and the powder was compressed against a polished steel plate to form a flat surface together with the sample holder (see Fig. 4).

Fig. 4. Cross section of specimen preparation devices. 1 is the steel bottom plate with highly polished upper surface, and 2 is the locking ring which keeps the sample holder 3 in place. The powder is poured into the holder through a filling device 4, which includes a coarse sieve 7 with frame 6. The powder in the holder, 9, is separated by a thin leaf, 5. The filling device is replaced by a guiding ring 8, and the powder is compressed by the punch, 10.
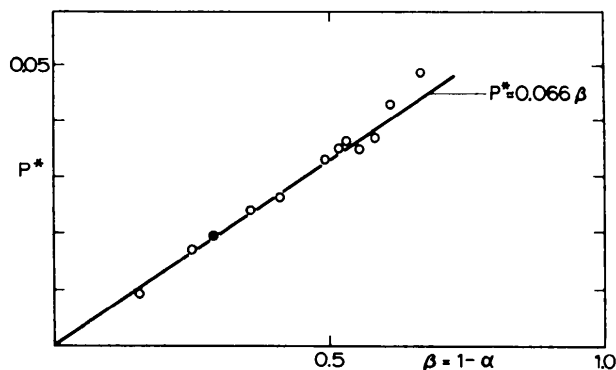

Fig. 5. Fractional reduction, P^*, of the fluorescent intensity as a function of the pore fraction β. If the relative density is α, then $\beta = 1 - \alpha$. The filled circle corresponds to the standard sample.

The actual packing of a powder sample can be inspected directly by preparing a metallographic section from it. The densification process has been studied extensively with this technique in powder metallurgy; in this context we only refer to a review article by Bockstiegel (1966). The homogeneity can also be studied by measuring the specimen fluorescence and Bragg intensities from different parts of the specimen.

The material for the powder standard was selected to be carbonyl process nickel, in fact the same powder that was used in the Powder Intensity Project. The main reasons for this choice were that the powder had proved to be very stable chemically, and that much of the necessary preliminary work had already been done. Also this choice was favored by the simple crystal structure (f.c.c.) and by the high intensity of scattering of Cu $K\alpha$ with practically no specimen fluorescence. The large correction for anomalous dispersion is immaterial in the case of an intensity standard, and it also effectively precludes all premature speculations of the physical significance of the resulting structure factors.

The powder was manufactured by The International Nickel Co., Inc., and is known as INCO 100. The particles are spherical in shape as a result of the carbonyl process, and the nominal particle size is 3 to 5 μm. The manufacturer's statements of the impurities were: 0·2 % C, 0·1 % O, less than 0·01 % Fe, and less than 0·001 % S.

2.2 Tests using varying compacting pressures

2.2.1 Granularity effects

The reduction in scattered intensity arising from porosity, surface roughness and other inhomogeneities has been discussed most recently by Suortti (1972). He was able to separate the two effects: for scattering angles in the range 30° to 160°, say, the porosity reduction is independent of angle but the other effects are not. A convenient way to make the measurement is to excite specimen fluorescence (having an absorption coefficient μ^*) with an incident radiation having a coefficient μ. If the ratio of intensity to that from a polished bulk sample is $1 - P^*$, then the reduction P_0 at some other wavelength with coefficient μ_0 is given by

$$P_0 = \frac{2\mu_0}{\mu + \mu^*} P^*, \tag{1}$$

so long as the various absorption coefficients do not differ greatly. From measurements on copper samples, Suortti suggested the formula $P_0 = 0\cdot42\mu_0\bar{d}\beta$, where $\bar{d}$ is a characteristic dimension of the particles and β is the pore fraction.

A series of specimens of the standard powder were prepared using various pelleting pressures and were examined with Mo $K\alpha$ as the exciting radiation. Those specimens pressed with more than 30 MPa ($= 306$ kg cm^{-2}) showed a negligible ($< 0\cdot5 \%$) angular dependence of the fluorescence and thus the porosity reduction P^* could be plotted as a function of β as shown in Fig. 5. Since the scattering experiments were to be performed using Cu $K\alpha$, and noting that both Ni $K\alpha$ and $K\beta$ fluorescence are detected, we have $\mu_0 = 435$ cm^{-1}, $\mu = 420$ cm^{-1}, $\mu^* = 515$ cm^{-1} (*International Tables for X-ray Crystallography*, 1974, p. 62), and the results can be expressed as $P_0 = 0\cdot061\beta$, which compares well to $P_0 \simeq 0\cdot065\beta$ given by Suortti's formula.

Note that a granularity effect which is independent of angle is not only a convenience in analyzing the data, it is also an indication that the sample is homogenous.

2.2.2 Reproductibility of the specimens

The lateral uniformity of the diffraction properties of the

specimen was studied by rotating the specimen stepwise about the surface normal and measuring the respective integrated intensities of the first three Bragg reflections. The amplitude of the fluctuations is shown in Fig. 6 as a function of the compression. The level of the statistical variation is reached at very high pressures, and it is clear that low-density specimens are not suited for quantitative measurements of the Bragg intensities.

When the sample is spun about the surface normal the lateral inhomogeneities are averaged out. The variation of the integrated intensities, as measured from different samples, is shown in Fig. 7. As there are only three specimens of each kind, the conclusions remain qualitative, but above 30 MPa the differences are less than $1\frac{1}{2}\%$. When this is compared with the fluctuations in Fig. 6 the vital importance of the specimen spinner becomes obvious. Similarly, increasing the illuminated area (with larger slits) was found to reduce the fluctuations in Fig. 6.

2.2.3 Preferred orientation

The pelleting process can introduce actual changes in the powder, affecting primary extinction, for example. But the greatest effect is on preferred orientation, and this problem is discussed here.

A sophisticated application of the Schulz (1949) method is described by Järvinen, Merisalo, Pesonen & Inkinen (1970). The pole density distribution is measured in the accessible region. This distribution is fitted with an appropriate harmonic expansion, which is then used to extrapolate to inaccessible regions. When the orientation pattern is simple only a few terms of the harmonic expansion are needed and they are determined by the lowest-order reflections (for an example, see Fig. 10). According to measurements on cubic and h.c.p. metals (Pesonen, Järvinen & Kurki-Suonio, 1973) a very simple pattern is obtained when the compacting pressure is large enough. Preferred orientation becomes well developed and regular, and even very large corrections (70% excess of intensity) can be made reliably.

The effect of preferred orientation on the first three reflections from the present Ni powder is shown in Fig. 8. Although

the inhomogeneities make the low-pressure values somewhat unreliable, the following things can be concluded:

– Even a very small pressure introduces noticeable preferred orientation. This is somewhat unexpected, since the powder particles are spherical in the present case, and there are no obvious easy orientation directions.
– At larger pressures preferred orientation behaves very regularly as a function of the pressure, for the 200 reflection it seems to saturate at 200 MPa.
– The standard deviation of the overall fit is about 0·6% and constant.

The general conclusion in respect of preferred orientation in the present case is that it is unavoidable and the best strategy is to press the specimen hard enough to make preferred orientation well developed and regular.
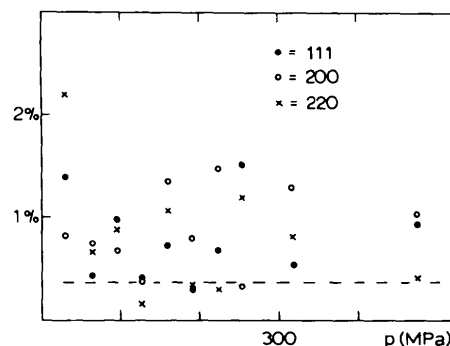

Fig. 7. Maximum differences between the integrated intensities from three samples of Ni, as a function of compression. The probable difference, 2σ, due to counting statistics is indicated by the broken line. The samples were spun about the surface normal at 30 r.p.m.

Fig. 8. Effect of preferred orientation on the integrated intensities of the first three reflections of Ni, given as a function of the compacting pressure p. W_{hkl} is the ratio of the measured integrated intensity – when the scattering vector coincides with the surface normal of the sample – to the average 'true' value. The quality of the fit to the cubic harmonic expansion is given by the standard deviation, σ, which is indicated by error bars.
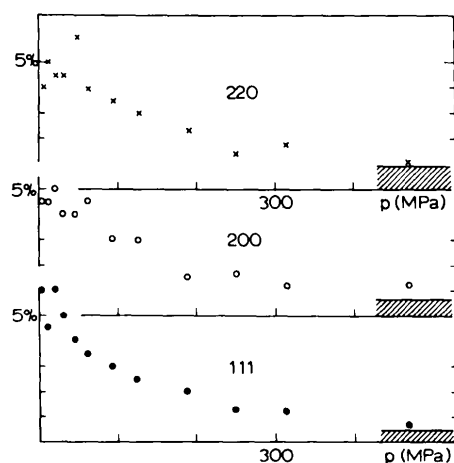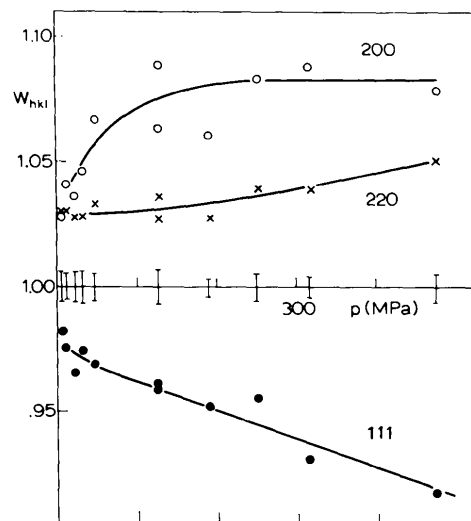

Fig. 6. Fluctuation of the integrated intensity when the sample is rotated about the surface normal. The points correspond to the range which includes 80% of the measured values, and the shaded band indicates the corresponding statistically probable range (about 3σ).

2.3 Standard sample

The most important factor in deciding on the standard was the uniformity of the scattering power across the face of the sample, so that the results would be independent of the
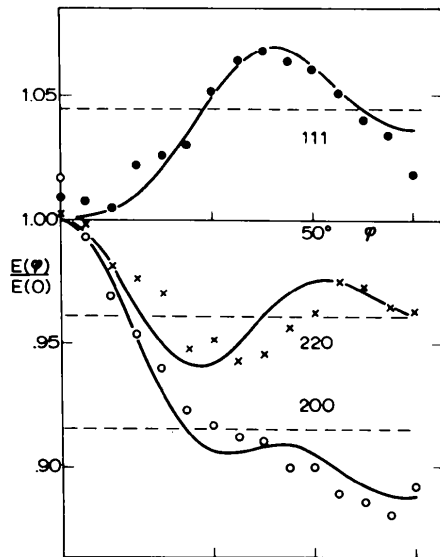

Fig. 10. Integrated intensities E_{hkl} of the first three reflections of the standard sample as functions of the tilting angle φ. The measurements are made in symmetrical reflection, and φ is the angle between the surface normal and the plane of diffraction. The experimental points are average values from measurements at φ and $-\varphi$. The full lines give the cubic harmonic fits to the experimental values, and the broken lines give the average 'true' values of each E_{hkl}.
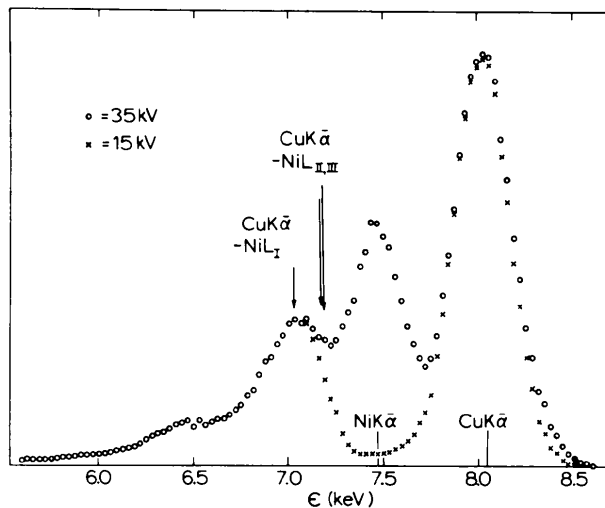

Fig. 11. Energy analysis of the background scattering from Ni at $2\theta = 30°$ with two different operation voltages of the X-ray tube: 35 kV and 15 kV. The spectrum exhibits (from the right): the combined peak of the TDS and Compton scattering, Ni K fluorescence (with 35 kV), anomalous or resonant Raman scattering, and Fe K (impurity) fluorescence.

cross section of the incident beam. Nevertheless, the use of a specimen spinner is strongly recommended to cut down the fluctuations in the intensity. The considerations of well developed preferred orientation and small and constant porosity effect also suggest selection of a hard-pressed sample. The disadvantage of such a sample is that the Bragg reflections broaden, and at the limit the separation of the reflections becomes difficult.

After weighing the above considerations, the standard samples were selected from those pressed at 250 MPa. Their main features are the following:

- A scanning electron micrograph of the surface of that sample is shown in Fig. 9.
- The relative density of the sample is 0·71. The effect of the sample porosity on the Bragg, thermal diffuse, and Compton scattering is 1·8 % (cf. Fig. 5). This is constant to better than 0·5 % over the range of measurement, $25° < 2\theta < 160°$.
- The effects of preferred orientation on the integrated intensities were determined by the method of Järvinen et al. (1970). The resulting corrections are given in Table 2, and the cubic harmonic fit is shown in Fig. 10.

The experimental values of the integrated intensities of the Bragg reflections of the standard sample, as given later, will not be corrected for the granularity effects and preferred orientation, but these corrections are needed for an adequate calculation of the Compton and TDS intensities.

Table 2. *Effects of preferred orientation on the integrated intensities of the Bragg reflections from the standard specimen pressed at* 250 MPa

W_{hkl} is the ratio of the measured integrated intensity – when the scattering vector coincides with the surface normal of the sample – to the averaged 'true' value.

hkl	111 222	200 400	220	311	331	420
W_{hkl}	0·9554	1·0834	1·0387	0·9808	1·0016	1·0155

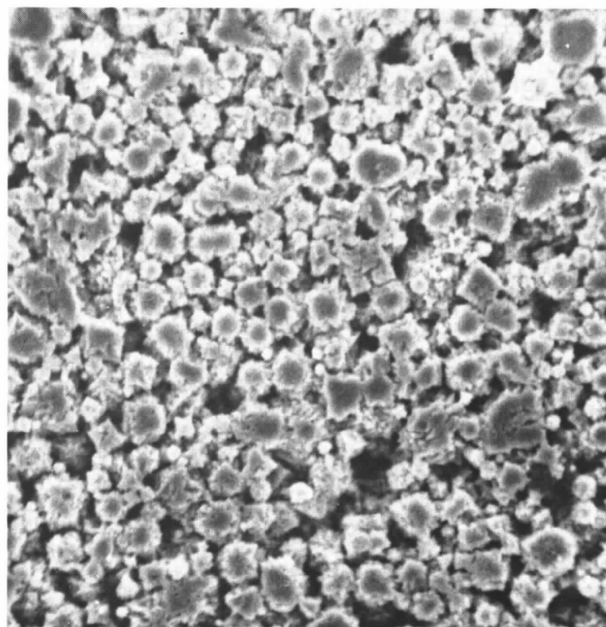## II. DATA REDUCTION AND ANALYSIS

II.1. Background components

The aim of this study is to separate the Bragg component from the total scattering. In principle, there is one possibility of doing this directly: the Mössbauer technique, which will be discussed later. At the moment, however, the practical way of separating the Bragg scattering seems to be a careful analysis and subtraction of the other components from the total.
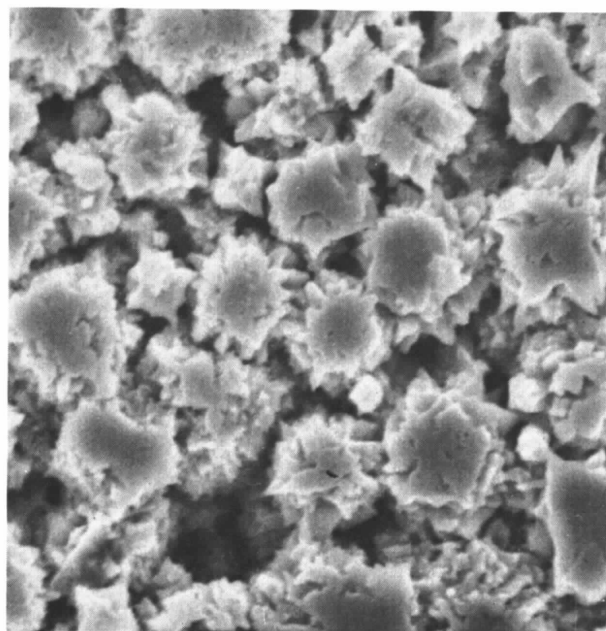
For the case of symmetrical reflection from a sample which intercepts the entire incident beam, the measured scattering can conveniently be related to the calculated values through the quantity

$$a_j \equiv \frac{n_j}{n_0 r_e^2 M_0 \Omega K_{\text{pol}, j}} = \frac{I_j}{\mu_0 + \mu_j}. \qquad (2)$$

The subscript j refers to various processes discussed below and the corrections alluded to earlier are assumed to be applied. The incident flux is n_0, n_j is the detected flux, μ_0 and μ_j the corresponding absorption coefficients, Ω the solid angle subtended by the receiving slit, r_e the electron scattering length, and M_0 the number of unit cells per unit volume. For an ideal powder sample the polarization factor $K_{\text{pol}} = (1 + K \cos^2 2\theta)/(1 + K)$ for the Bragg, Compton and thermal diffuse scattering; for fluorescence and other isotropic radia-

PLATE 79

(a)

(b)

Fig. 9. Scanning electron micrograph from the surface of the standard sample. Magnification in (a) is 1000× and in the blow-up (b) 3000×. The size distribution of the approximately spherical particles was estimated from a micrograph of a loosely packed sample, and the average chord length inside the particles, $\bar{d}$, was estimated to be 3.6 μm.

tion $K_{pol} = 1$. The scattered intensity in electron units, I_j, is referred to one unit cell. In usage appropriate to photon counting, I_j refers to the probability of an event; to obtain the energy transfer, multiply by the ratio $\varepsilon_j/\varepsilon_0$.

1.1 Energy analysis

The initial resolving of the components of the total scattering was done with an energy dispersive Si(Li) detector. An analysis of the background scattering under the normal operation conditions, 35 kV and 18 to 20 mA, is shown in Fig. 11. The various components are described briefly in the following, and the results of the resolving are summarized in Table 3.

Table 3. *Results of an energy analysis of the background scattering under normal operation conditions:* 35 kV *and* 20 mA

The measured contribution of the Ni and Fe fluorescences and the anomalous scattering are denoted a_{Ni}, a_{Fe}, and a_{anom} (*cf.* equation 2). These measured values need to be corrected for the additional absorption between the sample and the scintillation crystal arising from the wavelength shift. The true values are denoted $a_{0, Ni}$, *etc.*

	Ni *K*	Fe *K*	Anomalous
$a_j \times 10^3$ cm^{-1}	5·23	0·27	5·75
$a_{0,j} \times 10^3$ cm^{-1}	5·62	0·38	7·37
$(\mu_0 + \mu_j) \times$ cm	950	1223	1132

1.1.1 Slightly modified scattering

The peak at 8 keV is due to the TDS, plasmon and Compton scattering. These cannot easily be resolved with an SSD and will be discussed in § 1.2.

1.1.2 Specimen fluorescence

The peak at 7·5 keV is the Ni $K\alpha$ fluorescence excited by the harmonic components of the primary beam; the Ni $K\beta$ peak is at 8·3 keV. Another measurement was made with the operation voltage changed to 15 kV, where the Ni K fluorescence is eliminated (crosses in Fig. 11). There is also a small bump at 6·4 keV, which arises from the iron impurity; the iron content was estimated to be order of 0·01 %, in agreement with the manufacturer's statement.

1.1.3 Anomalous scattering

The component which peaks at 7 keV and has a long low-energy tail is so-called anomalous or resonant Raman scattering. It has an appreciable cross section only when the energy of the incident radiation is just below an absorption edge of the sample: here $\varepsilon_{Ni K} - \varepsilon_{Cu K\alpha} = 290$ eV. In the visible-light region the resonant Raman scattering has become an effective tool for studies of band structures (Cardona, 1974). At X-ray energies, this scattering was first reported by Sparks (1974). It is interpreted as a two-electron process, where the incident photon virtually excites a K-shell electron (in this case) and a photon is simultaneously emitted with an L-shell electron. As a result, there is a photon of modified energy, $\varepsilon = \varepsilon_{Cu K\alpha} - \varepsilon_{Ni L} - \varepsilon_{kin}$, and an electron from the L shell with energy ε_{kin}.

A separate study of the anomalous scattering was made by one of us (P.S.); this will be published elsewhere. The following findings are relevant to the present work:

- Anomalous scattering is isotropic and unpolarized within the experimental accuracy.
- The scattering cross section for Ni at Cu $K\alpha$ radiation is $I_{anom} = 8·55$, and after correction for the porosity reduction, 8·35 for the standard sample.

- The average energy of an anomalously scattered photon is 6·7 keV, which gives $\varepsilon_{anom}/\varepsilon_0 = 0·83$.

1.2 Separation of incoherent scattering

The various scattering processes are characterized by the entity accepting the momentum and energy transfers, Δk and $\Delta \varepsilon$. For Bragg scattering Δk is absorbed by the average lattice and $\Delta \varepsilon \simeq 0$; in the TDS the interaction is with the vibrating atoms, and $\Delta \varepsilon$ is from 0 to 0·1 eV; in the plasmon scattering collectives of electrons are involved, and $\Delta \varepsilon \simeq 10$ eV; and finally, in the Compton scattering Δk is carried by one electron with an energy change of order 10 to 10^2 eV. The plasmon and Compton contributions can be resolved from the other components with a crystal spectrometer, but this is very hard to do on an absolute basis; separation of the TDS is yet more difficult. Thus, from the practical point of view, these contributions must be estimated theoretically.

1.2.1 Plasmon scattering

Plasmon scattering has been recently reviewed by Platzman (1974). The agreement between the theory and the experiments is only qualitative at the moment and so reliable estimates of the scattering are not available. The gross features of this scattering are the following:

- The scattering is strongest at small angles (small Δk), where it is of the same order of magnitude as the Compton scattering.
- The energy shift is almost constant, increasing only slightly with the scattering angle, in contrast to the Compton scattering.

In the present case no attempt was made to estimate and subtract the plasmon contribution from the total scattering.

1.2.2 Compton scattering

Although the Compton scattering from a free electron is well understood and the Compton scattering from a tightly bound electron is negligible, the best present-day calculations may entail a relative error of the order of $(\varepsilon_B/\Delta\varepsilon)^2$ for intermediate cases, where ε_B is the binding energy. These calculations may be based on Waller–Hartree (WH) theory (Waller & Hartree, 1929; Freeman, 1959), on the impulse approximation (IA) (Platzman & Tzoar, 1965; Eisenberger & Platzman, 1970; Currat, DeCicco & Weiss, 1971) or modifications of these approximations (Paakkari & Suortti, 1974). The discussions are given in terms of the cross section $(d\sigma/d\Omega)_C = I_C r_e^2$, or the differential cross section $(d\sigma/d\Omega d\varepsilon)_C$. Measurements of the latter give valuable information about the electronic states; for references see Stevens (1973).

There are only a few measurements of total Compton cross sections (Walker, 1956; Weinberg, 1964; Paakkari & Suortti, 1974), but these show that the errors in the theoretical calculations may be of the order of one electron unit per atom, which is larger than the typical experimental accuracy. In spite of this limitation, we made an estimate of the Compton scattering for nickel. The WH calculations of Cromer (1969) are shown as the full curve in Fig. 12. According to the IA, these should be corrected by the factor $\bar{\varepsilon}/\varepsilon_0$, where $\bar{\varepsilon}$ is the average Compton-shifted energy. In our geometry, account must also be taken of the increase of the absorption coefficient, μ_C, with the scattering angle. These two corrections are incorporated in the broken curve of Fig. 12.

1.3 Thermal diffuse scattering (TDS)

Because of the peaking of the TDS at the positions of the Bragg reflections, it is very important to have an accurate

assessment of its magnitude. It is possible to separate the elastic scattering from the TDS (and other inelastic scattering) by means of the Mössbauer effect (e.g. O'Connor & Butt, 1963; Albanese & Ghezzi, 1973), but the small available intensity and other difficulties preclude making accurate, absolute measurements on powders with this technique. Thus the practical method is to separate the TDS on the basis of a calculation. Note, however, that because of the shape of the TDS, it is possible to make some checks on the calculation if the scattering is measured at all angles, and further checks are possible if the temperature dependence of the diffuse scattering is measured.

Several techniques are available for making nearly exact calculations in the quasi-harmonic approximation (Paskin, 1959). The most usual method is to expand in the quantity $M = B(\sin \theta/\lambda)^2 = 8\pi^2 \bar{u}^2 (\sin \theta/\lambda)^2$, where $\bar{u}^2$ is the mean squared amplitude of vibration of an atom. Taking the simple case of a monoatomic crystal for illustration, the TDS is

$$I_{TDS} = f^2 e^{-2M} \sum_{l=1}^{\infty} \frac{(2M)^l}{l!} \zeta_l(S).$$ (3)

The lth term in this expansion can be shown to correspond to exchange of energy and momentum with l phonons. Expressions for $\zeta_l(S)$ can be written down in terms of the quantities which characterize the phonon spectrum (Cochran, 1963; Pawley, 1969). With certain approximations, the average of each ζ_l over a unit cell in reciprocal space is unity,
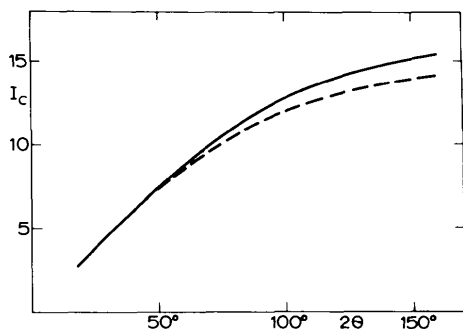

Fig. 12. Compton cross section of a Ni atom in electron units. The full curve is the theoretical result for zero wavelength shift (Cromer, 1969), and the broken curve is appropriate to a Cu Kα incident beam.
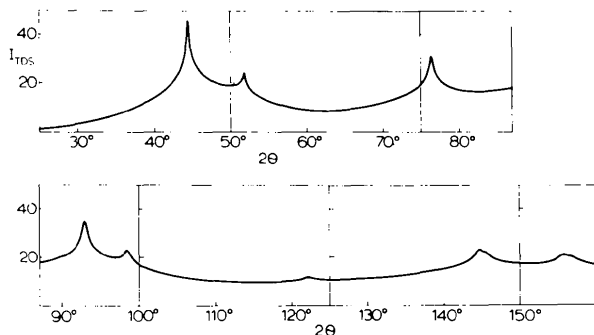

Fig. 13. The angular dependence of the TDS intensity as convoluted by the instrument function. Values are in electron units per atom.

and the average value of I_{TDS} is $f^2(1 - e^{-2M})$ (Guinier, 1963; Borie, 1961). Equation (3) can be adapted to powder usage by averaging ζ_l over a sphere of radius $S = 2 \sin \theta/\lambda$. This average may be denoted $C_l(S)$, and an appropriate average of C_l over a range of S is also approximately unity.

For some materials, the phonon spectrum is well enough known that several C_l could be calculated to the required accuracy. The concomitant computer effort would probably not be impossible, but is so large that all calculations to date have involved approximations. We will not discuss these in detail, but instead refer to some recent work where additional references may be found (Walker & Chipman, 1972). There have been a few experimental checks of these calculations (Chipman & Paskin, 1959a) and one may also compare the results of various models. Such checks suggest that the errors, for temperatures comparable to the Debye temperature, may be in the range of 5 to 20%.

As an indication of present-day methods, we outline the calculation used here for nickel (Suortti, 1977), the results of which are shown in Fig. 13.

1. In the case where many phonons are involved in the scattering, most of the structure of ζ_l, and yet more so of C_l, is averaged out. Thus, for $l > 2$, we replace C_l by its approximate average, unity, and equation (3) becomes

$$I_{TDS} = f^2 e^{-2M} \left\{ C_1 \times 2M + C_2 \times \frac{(2M)^2}{2!} + \left[e^{2M} - 1 - 2M - \frac{(2M)^2}{2!} \right] \right\}.$$ (4)

2. The one-phonon function C_1 is calculated from the model of Walker & Chipman (1972), which takes long-wavelength phonons into account exactly but makes use of approximate relations for high-frequency phonons. The elastic constants were selected in the way which gave the best fit of the model to the experimental dispersion curves (Birgeneau, Cordes, Dolling & Woods, 1964): $c_{11} = 2\cdot37$, $c_{12} = 1\cdot41$, $c_{44} = 1\cdot16$; in units of 10^{11} Nm^{-2}. The first-order TDS has the same shape around each modified scattering vector as the Bragg scattering does around the reciprocal-lattice vector (e.g. Warren, 1969). Thus the effects of geometrical aberrations, particle size, strain and wavelength broadening, etc. can be taken into account by convoluting the observed Bragg profile with the 'ideal' TDS (Suortti, 1967; Bradaczek & Hosemann, 1968).

3. An isotropic model is used for calculation of C_2 (Suortti, 1974). The contributions of $K\alpha_1$ and $K\alpha_2$ were calculated separately, but no further convolution by the instrument function was found necessary.

4. The value of $B = 0\cdot38$ Å^2 was taken from the results of Paakkari (1974). Values of f can be taken from the present experiments in which case many of the corrections, e.g. dispersion and granularity, are taken care of automatically. But it is more convenient to make the corrections to tables of smooth values (International Tables for X-ray Crystallography, 1974, p. 79). The dispersion correction, $f' = -2\cdot99$, was taken from a measurement by Materlik (1975), and the other corrections were evaluated from the present study.

5. Preferred orientation changes the powder TDS in a very complicated way. Near the reflections the changes follow those in the Bragg intensities, but in the regions between the reflections the TDS comes from reciprocal-lattice points which are away from the direction of the scattering vector. In the specimen these correspond to directions which are away from the surface normal, where the pole densities of the

crystallographic directions have either maxima or minima (cf. Fig. 10). The changes of intensity due to preferred orientation are roughly proportional to the distance, $|S - S_{hkl}|$, from the surface normal, and this situation was approximated by a weight factor,

$$W = (1/\Sigma p_{hkl}) \sum_{hkl} p_{hkl} \left\{ W_{hkl} - \frac{|S - S_{hkl}|}{g_m} (W_{hkl} - 1) \right\}, \quad (5)$$

which was applied to the calculated TDS intensity. The summation includes the reflections hkl for which $|S - S_{hkl}| < g_m$, the average radius of the Brillouin zone, and p_{hkl} is the multiplicity of the reflection. W_{hkl} is given in Table 2.

In addition to errors introduced by the simplifications in the model, there may be errors arising from the neglect of anharmonic terms. These have been studied in the case of single crystals (e.g. Pirie, Reid & Smith, 1971; Hervet & Ober, 1973; Albanese & Ghezzi, 1973), but there is yet no generally agreed technique for handling them. The effects are assumed to be small in the case of a powder average, and they are neglected here.

We conclude with a brief remark about the widely used Chipman–Paskin (1959b) approximation for the TDS included above a straight-line background. This included TDS is a linear function of the length of scan if the contributions from all neighboring Bragg reflections are removed. But Fig. 13 shows that it would be a complex task to remove these other contributions, and it is thus preferable, with computers so readily available, to make a more exact calculation of the form of the TDS as has been done here.

II.2. Bragg intensity

2.1 Widths of the reflections

The analysis of a typical angular region is illustrated in Fig. 14. First the experimentally determined contributions to a (equation 2) are removed. These include fluorescence, anomalous scattering, detector noise, cosmic rays, perhaps slit or air scattering, etc. The remaining scattering is shown in the figure. Also shown are the calculated values for TDS and Compton scattering, making use of $\mu_0 = 435$ cm^{-1}, and the final values for a after subtracting these two contributions. The following features may be observed:

- The calculated TDS plus Compton scattering explains most of the background intensity. This holds for the whole range of measurement, although not shown in the figure.
- There is a small, almost angularly independent residual. Part of this is explained by multiple scattering (Suortti, 1975), as shown in Fig. 15. The peak between 88° and 89° is identified as the doubly diffracted 111 reflection. The remainder of the residual arises from sample non-idealities as discussed in § II.3, and/or from uncertainties in the calculated values, especially of the Compton scattering.
- Because the residual scattering is a smooth function of angle, it is possible to separate the Bragg pair; the small peaks of the double scattering can be separated according to Fig. 15. It is also possible to separate the individual peaks with reasonable accuracy by extrapolation through the overlap region.
- The actual widths of the reflections are very large, of the order of 7° in the present case. A comparison with Fig. 16 is revealing; in that figure a conventional straight background is drawn for the reflections separately. As a result the shaded part in Fig. 14 would be lost from the Bragg intensity. This corresponds to 2·7 and 3·4 % losses of the integrated intensity in 311 and 222 respectively.
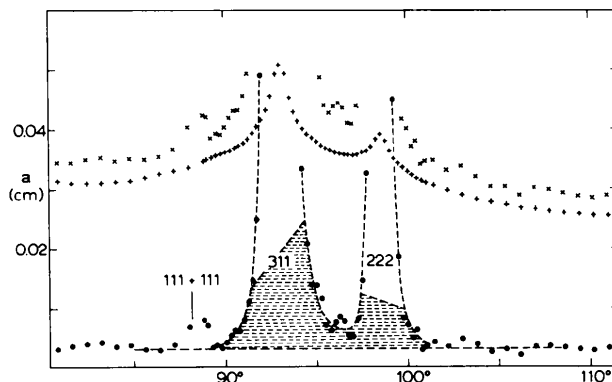

Fig. 14. Scattering cross section in the vicinity of 311 and 222 reflections; the measurement is on a Ni sample pressed at 130 MPa. The total scattering (minus the constant contributions of the anomalous scattering and specimen fluorescence) is given by crosses (×), the sum of the TDS and Compton scattering by upright crosses (+), and the Bragg plus residual scattering by filled circles (●). The doubly diffracted 111 reflection is indicated, and the shaded area represents the intensity which is lost in a conventional separation of the background (see Fig. 16); this is 2·7 % of E_{311} and 3·4 % of E_{222}.
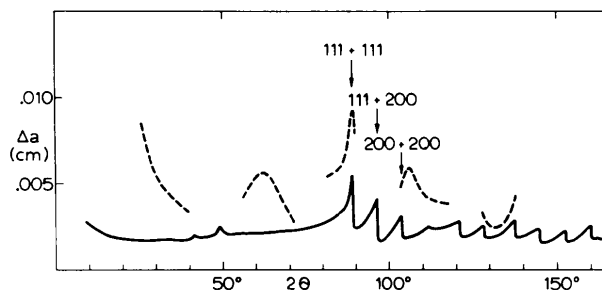

Fig. 15. Residual scattering from a Ni sample pressed at 130 MPa outside the Bragg reflections in units of $1/2\mu_0$ (broken line, cf. equation 2). The calculated intensity of the double scattering is given by the full curve, and some combinations of the double reflections are identified.
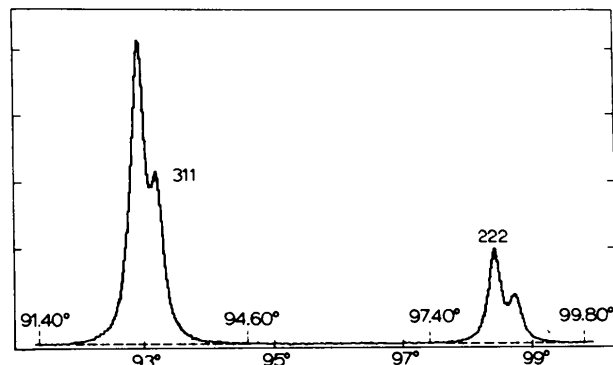

Fig. 16. Step scan of the 311 and 222 reflections of a Ni sample pressed at 130 MPa. The receiving slit is 0·1 mm (0·03°) and the step 0·02°. The broken line gives a conventional separation of the background.

– It must be realized that the 311–222 pair is still a rather easy case. At larger values of $\sin\theta/\lambda$ the reflections begin to overlap continuously, and the actual background could not be found at all without an analysis as exemplified here.

2.2 Integrated intensities

As mentioned earlier, the integrated intensities of the Bragg reflections were measured by a stationary, 4·0° wide receiving slit. The intensity in the tails was calculated from plots like Fig. 14, which were also used for determination of the end-points of the reflections. The background was measured at these points (actually at several points nearby) and
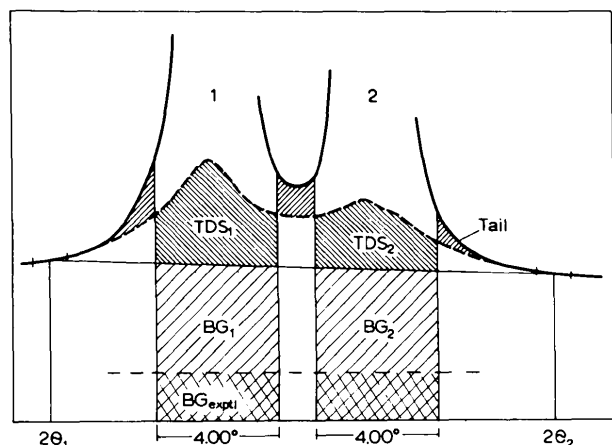

Fig. 17. Schematic picture of the various contributions in a measurement of the integrated intensity. There are indicated the Bragg intensity within the 4·00° slit and its tails outside that slit, the included TDS, background due to nearly elastic scattering (BG), and the experimentally determined background (BG_{expt1}). For our apparatus this latter includes detector noise, specimen fluorescence and anomalous scattering and is angularly independent; in other cases it might include angularly dependent air and/or slit scattering.

it was subtracted from the integrated intensities using linear interpolation. The included TDS was calculated by numerical integration. The overlapping tails of the reflections were separated graphically. The various contributions are shown in Fig. 17.

In the ideal powder approximation (Warren, 1969), the corrected measured Bragg power can be related to sample properties through

$$E_{hkl} = \frac{n_{hkl}}{n_0 r_e^2 M_0 \varphi K_{pol, hkl}} = \frac{M_0 \lambda^3 p_{hkl}}{8\pi \sin\theta_{hkl} \sin 2\theta_{hkl}} \cdot \frac{f_{hkl}^2 e^{-2M}}{2\mu_0}, \quad (6)$$

where φ is the (corrected) planar angle intercepted by the slit height; M_0 and f refer to the monoatomic unit cell. The experimental results can equally well be presented as values of E_{hkl} or $f_{hkl}^2 e^{-2M}/2\mu_0$, since all other quantities in the latter formula are well known. Such results for the standard sample, along with various corrections and values for the numerical factors, are collated in Table 4.

II.3. Relation of integrated intensity to structure factor

The discussion so far has mostly centered on the problem of separating the Bragg scattering from other power recorded by the detector. There remains the difficult problem of determining the structure factors from the observed Bragg scattering. Many of the ramifications of this problem are beyond the scope of the present review, but some aspects are so intimately linked with the experimental problem that it is appropriate to discuss them here. In particular, we have assumed that it is feasible to separate the Bragg scattering associated with each Bragg peak. It is also assumed that the relationship of integrated reflection to the structure factor is given by equation (6). We want to discuss these assumptions briefly.

3.1 Extinction and broadening losses

For simplicity, consider for the moment an ideal powder sample consisting of platelets whose faces are parallel to the active diffracting planes. Although, in practice, slits of varying

Table 4. Measurement of the integrated Bragg reflections from the standard Ni sample pressed at 250 MPa

The integrated power is given by $E_j = \int a_j d(2\theta)$, cf. equations (2) and (6), and the various quantities are defined in Fig. 17. The values of E_{hkl} and thence $f^2 e^{-2M}/2\mu_0$ are corrected for dead time, polarization factor and similar apparatus effects, but not for preferred orientation, porosity and similar sample effects. Except for small differences in sample preparation, the values may thus be compared directly to the results of the Powder Project (Jennings, 1969), but do not reflect fundamental properties of nickel metal.

				Integrated power $\times 10^3$ cm^{-1}						
hkl	$2\theta_{hkl}$	$2\theta_1$	$2\theta_2$	4·0 slit*	BG†‡	Tails	TDS	E_{hkl}**	p_{hkl}	$\dfrac{f_{hkl}^2 e^{-2M}}{2\mu_0}$
111	44·53	39·00		129·78	1·89	0·22	1·26	126·85±0·22	8	0·3158
200	51·89		56·00	72·66	1·94	0·24	0·53	70·43±0·23	6	0·3029
220	76·44	71·50	80·50	45·85	2·42	0·13	0·54	43·02±0·17	12	0·1618
311	93·02	87·00		50·93	2·63	0·30	0·74	47·86±0·16	24	0·1084
222	98·53		102·00	16·47	2·56	0·03	0·34	13·60±0·09	8	0·0955
400	122·08	117·00	126·50	9·25	2·13	0·16	0·06	7·22±0·05	6	0·0669
331	144·91	137·33		30·13§	2·29	1·58	0·46	28·96±0·30	24	0·0494
420	156·06		162·40¶	34·68§	2·16	4·63	0·34	36·81±0·60	24	0·0458

* Constants used in the calculations: $r_e^2 M_0 = 7·2577 \times 10^{-3}$ cm^{-1}, $\lambda = 1·54166$ Å, $a_0 = 3·5239$ Å, $B = 0·38$ Å^2, $f' = -2·99$, $\mu_0 = 435$ cm^{-1}, $T = 298$ K.

† The angularly independent quantity, $BG_{expt1} = 0·79 \times 10^{-3}$ cm (cf. Fig. 17 and Table 3), has been separately subtracted.

‡ BG = background, +0·2% correction for geometrical aberrations made.

§ Geometrical correction of −0·15% made to the Bragg intensities.

¶ End-point, the background value, and the tail contribution above 160·00° estimated.

** Estimated errors include uncertainties in the background level, in the tail contribution, and in the photon counting. In addition, there is an overall uncertainty of 0·3% in the absolute scale and a small possible error (less than 0·2%) in the polarization factor, K_{pol}.

sizes will be used for the measurements, it is simplest to consider the Bragg power $i(s)$ detected by a fine slit, where s is the deviation of $2 \sin \theta / \lambda$ from the Bragg condition. The complete formula for $i(s)$ is known (Wilson, 1962; Guinier, 1963), but we require only the integral breadth $\beta_s = 1/T$ and the average value at large s,

$$i(s) \simeq \frac{N_{hkl}}{2\pi^2 L s^2} \text{ (asymptotic average)}. \qquad (7)$$

In these expressions T is thickness of the platelets, the integrated reflection $N_{hkl} = \int i(s) \mathrm{d}s$ is related through geometrical factors to the quantity in (6), and L is the volume of a mosaic crystallite divided by the area of its projection on the reflecting plane. For our simple model, $L = T$.

From the above formula it is a simple matter to calculate the loss in the measured integrated reflection if the scan is carried out only from $-s$ to $+s$, say. Typically, this loss has two components; the neglected wings and also an amount that is subtracted because the measured 'background' is too high. These two contributions are equal, and the total loss in the integrated reflection on account of broadening is

$$(\Delta N_{hkl}/N_{hkl})_b = 2\beta_s/\pi^2 s. \qquad (8)$$

Thus one may see that if an error of 5% is tolerable, a scan equal to about eight integral breadths is required, but for an accuracy of 0·1%, a scan of over 400 integral breadths is necessary.

The maximum permissible scan is limited by the occurrence of neighboring peaks. So for example, if it is required that only 0·1% of the integrated reflection is left outside the maximum scan, it would be necessary to use particles so large that the integral breadth was of the order of 1/400 of the spacing between the peaks. Such large particles give rise to primary extinction, however. In the present example, and considering only the σ polarization, the leading term in the fractional reduction in integrated reflection arising from primary extinction is

$$(\Delta N_{hkl}/N_{hkl})_e = (r_e \lambda F/\beta_s V_c \sin \theta)^2/3, \qquad (9)$$

where F is the structure factor and V_c the volume of a unit cell. Note that, for a given reflection, this result is approximately independent of wavelength.

To illustrate the importance of these ideas, consider the case of MgO powder. Because the spacing between 111 and 200 reflections is only $0·268/a_0$, where a_0 is the lattice parameter, it is only possible to scan out to about $s = 0·134/a_0$ from either of these reflections. The total error for such a scan can then be calculated from equations (8) and (9) for any value of the breadths β_s (i.e. for any thickness of the platelets). The percentage loss so calculated for the 200 reflection is plotted vs T in Fig. 18. Note that the loss is always greater than 0·9% and that for a range of particle thicknesses the loss would be even greater. For other cases the situation is even more dramatic. The minimum loss is 1·3% for nickel and about 3% for gold. A careful analysis of the background may make it possible to estimate a correction for the broadening loss, as discussed in § II.2, but corrections for extinction are even more difficult.

The model used has two simplifications: the use of platelets and the consideration that each particle is completely independent of all others. This latter condition is quite significant and will be discussed later. The restriction to platelets, on the other hand, is thought to be of little consequence. If one were to consider instead spherical particles, for example, equation (8) would be changed by only a factor of $\frac{8}{9}$. Physical reasoning

indicates that equation (9) would be changed by a similar factor so that the overall appearance of Fig. 18 would not alter greatly. For other particle shapes, the changes would be somewhat more, but not drastically more for particles of reasonable shape.

3.2 Other losses

The relationship between integrated reflection and structure factor given by equation (6) is valid in the ideally mosaic model. This model assumes a large number of completely independent small particles each of which is composed of a perfect lattice. In addition to primary extinction arising from interactions within a mosaic, there may be effects on the integrated reflection arising from the lack of independence of the mosaics. We present here some results and discussion which appear to show the importance of such effects.
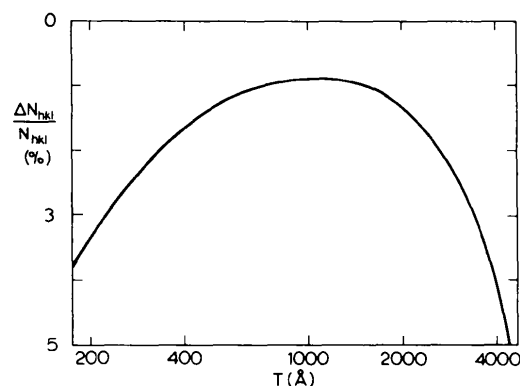

Fig. 18. Percentage loss in integrated reflexion vs particle size for MgO 200. The scan extends from a position midway between 111 and 200 to the symmetric position on the other side of 200. The only losses considered are from line broadening and primary extinction.
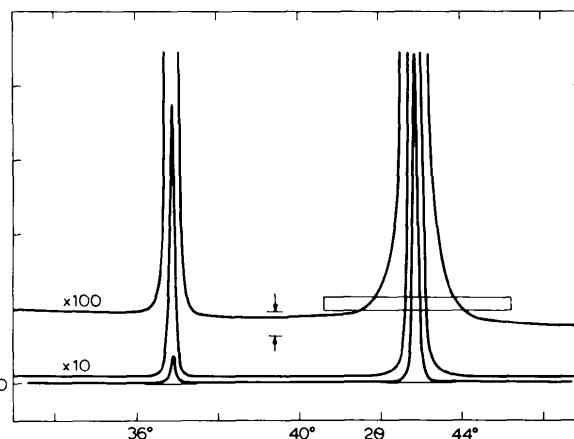

Fig. 19. A scan in the neighborhood of 111 and 200 for one of the MgO samples studied. The rectangle contains, on the most magnified scale, 1% of the area of 200. The range of intensity minima between the peaks, for the various samples studied, is shown by the arrows. In spite of being in the upper portion of this range, the sample shown displays a nearly flat background. This is evidence for amorphous scattering.

3.2.1 *Line profile measurements on* MgO

Some years ago, one of us (L.D.J.) undertook to measure the structure factors of MgO. Fig. 19 shows a scan through the 111 and 200 peaks for one of the many samples studied. Because of the small TDS in this material, the region between the Bragg peaks is relatively flat. It thus appears that it would be easy to separate the Bragg power. This ease is emphasized by the superimposed rectangle which has an area (on the most magnified scale) of 1% of the 200 peak. Of course, the situation is somewhat more difficult for the 111 difference peak which is only about $\frac{1}{10}$ as large, and there is detectable curvature midway between the peaks on a sufficiently enlarged scale. Nevertheless, with techniques discussed in § II.2, it is possible to evaluate the integrated reflection (with background, including TDS, removed) for the low-order reflections.

Such measurements were made on a number of samples which had undergone various grinding and annealing procedures. Unfortunately some of these procedures resulted in samples which displayed appreciable preferred orientation. But we found that by suitable normalization and then averaging over 111, 200, and 220, most of the effects of preferred orientation could be removed. Although more accurate results could have been obtained using the more complicated procedures discussed earlier, the values obtained were adequate for the present qualitative considerations. Furthermore, an indication of the particle size is given by the full width at half maximum (FWHM) of a low-order peak, the 200 say. Thus the curve of normalized integrated reflection *vs* FWHM shown in Fig. 20 should be qualitatively comparable to the curve shown in Fig. 18. (Note that the abscissa is reversed; large peak widths correspond to small particles.) The few samples with very narrow peaks showed such large extinction that it was not possible to include them in Fig. 20. Nevertheless one might hope that a quantitative comparison of data such as those shown in Fig. 20 with curves such as shown in Fig. 18 could yield an idealized integrated reflection which could then be associated with a correct structure factor through equation (6). Attempts to carry out such a comparison met with fundamental difficulties which are now described.

Semiquantitative estimates of the particle size could be made on the basis of the reduction in integrated reflection, on the basis of the FWHM of the peak, on the basis of the scattering far from the peak (for example, midway between the widely separated 200 and 220), and on the basis of scattering at intermediate distances from the peak. It was found that these various estimates of particle size were completely inconsistent. We therefore determined to make a full investigation of the line profiles to elucidate these inconsistencies.
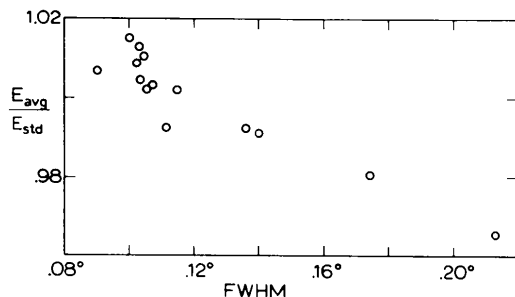

Fig. 20. The normalized, averaged integrated intensity of MgO 200 as a function of FWHM for a number of the samples studied.

Three representative samples were selected and studied with monochromated Cu $K\alpha$ radiation. A variety of slit systems was used so as to optimize the resolution for small s and to obtain large count rates at large s. In each case the data were normalized by the integrated intensity measured with the same slit system (or as calculated from receiving slit dimensions and a stationary-slit measurement). In those cases where the maximum resolution was required, the data were first corrected for the 7% α_2 contamination with the scheme of Rachinger (1948). The resulting line shape was then corrected for specimen transparency with the technique of Keating & Warren (1952), using absorption coefficients actually measured for each sample. Finally corrections were made for flat-specimen broadening, slit widths, axial divergence, *etc.* by using an iterative deconvolution procedure in conjunction with data taken on a hot-pressed MgO sample. Although this standard sample gave peaks that were almost completely determined by instrumental broadening, it is important to note that any particle-size broadening in the standard would give rise to narrowing of the deconvoluted peak for the sample. An indication of the extent of the deconvolution is given by the FWHM values of Table 5.

Table 5. *Some parameters for the* MgO *samples reported*

Sample	A	B	C
L (Å)	300	1400	6000
FWHM (°)			
data	0·200	0·110	0·080
standard	0·062	0·055	0·055
deconvolution	0·161	0·072	0·03
Averaged, normalized integrated intensity	0·97	1·01	1·11

The line profile so constructed contains the non-Bragg components previously discussed. Of these, only the TDS has appreciable curvature within the angular range of interest. An upper limit on this TDS could be established from measurements on the hot-pressed standard. In the range of angular deviations beyond about one degree from the Bragg peak, this upper limit was in close agreement with the calculated values. At smaller angular deviations the included TDS was inappreciable compared to the Bragg scattering and was thus of no great concern. Therefore the calculated TDS could be removed from the deconvoluted line with confidence. The residual linear background was taken into account as described below.

3.2.2 *Analysis of line profiles*

Diffraction line profiles are often discussed in terms of Fourier coefficients, as outlined below. For our purposes, however, the most revealing way to depict the Bragg line shape is to plot the quantity

$$G = 2\pi^2 s^2 i(s)/N_{hkl} \qquad (10)$$

as a function of s, or of the angular deviation from the Bragg condition, $\Delta 2\theta$. We can see from equation (7) that G has the asymptotic value

$$G_{as} = 1/L. \qquad (11)$$

In the real case where the powder sample is not composed of identical crystallites, the effective value of L is obtained by averaging over the diffracting particles. Two illustrative calculated cases are shown in Fig. 21, where it may be seen that the asymptote is effectively achieved for $s > 1/L$. The

plot of G vs s has the important property (Wilson, 1962) that for ideally mosaic samples the actual area under the experimental or calculated curve (starting from $s = 0$) must be less than or equal to the rectangular area indicated in Fig. 21. The difference in these two areas is related to the taper parameter and is zero for curve S and relatively large for curve P.

For each sample studied, plots of $G(s)$ were prepared for various assumed values of the residual linear background. In each case, there was a value of assumed background which yielded a sensibly horizontal asymptote, and Fig. 22 shows the plots using the appropriate background for each sample. Other choices of background yield increasingly large slopes at large s, as exemplified by the dot–dashed line for sample A. Thus the choice of the background is well determined.

It is immediately obvious that the results depicted in Fig. 22 cannot be given by ideally mosaic samples. As indicated by the dashed lines, much too much area is enclosed before the asymptotic value is attained. (Note that, for clarity, the origin for each curve is shifted by 0·25°.) The effect is proportionately greater for the samples with larger particle size. Note, however, that the effect is not caused by extinction; the received power is too small in the wings of the reflection where the extinction would be a minimum. We will discuss a few ramifications of the situation, but the important fact is that the measured results are impossible for samples which are nearly ideally mosaic.

Although the excess area is not accounted for in the ideally mosaic model, the excess is well known. It is attributed to strain and other imperfections. For sample B, for example, the effect of any reasonable taper parameter would be negligible, and the mean square strain would be 2×10^{-3}. Such effects have been studied in great detail in a large number of cases (Wagner, 1966), but there is no universal, generally agreed interpretation, and it is unclear how accurate an approximation is given by equation (6) when these effects are appreciable.

Customarily the analysis of the line shape $i(s)$ is carried out in terms of the Fourier coefficients $A(t)$; for recent references see Mitra & Chaudhuri (1974) and Gangulee (1974). This procedure has the ostensible advantage that the convolutions and deconvolutions in s are simple products and quotients in t and also there are simple relations between t and the spacings in the specimen. Thus, in principle, the effects of instrumental broadening are easily removed. The residual coefficients can then be compared with the results of sophisticated calculations based on various models. These models incorporate the effects of particle size, strain, faulting, $etc.$ Because of inadequacies in the data, in the model of the sample, or in the model of the diffraction process, it is not usually possible to obtain extensive results. For example, it is usually impossible to obtain a meaningful particle size distribution. Instead, one characterizes the model with a few parameters: average particle size, mean strain, faulting probability, $etc.$ Since faulting gives rise to an effective particle size (which depends on the hkl values), the two effects may be included together. They give rise to $A(t)$ which drops off linearly with t at small t. Strain, on the other hand, gives rise to $A(t)$ which drops off quadratically with t and also quadratically with n, the order of the reflection. These differences allow a separation of the various effects. It is not always emphasized, however, that these differences can be directly related to the experimental $i(s)$. So long as the strain contribution drops off more rapidly than s^{-3} (or for any bounded strain distribution) the linear term in $A(t)$ is given precisely in terms of the parameter L determined from the data at

large s (equation 11). Viewed in these terms, it is easy to see that the linear term in $A(t)$ does not depend strongly on the deconvolution of the instrumental broadening, but depends completely on the inverse square drop-off of $i(s)$ at large s. Thus it is far easier to find L from the $i(s)$ data than from the linear term in $A(t)$, which must be determined analytically ⸱ from an extrapolation to large s in any case.

3.2.3 Implications of the analysis

The asymptotes of Fig. 22 can be converted to L values with equation (11) and the results are given in Table 5. As previously remarked, these values are completely insensitive to the deconvolution procedure. Therefore it is appropriate to compare the losses in the integrated intensity predicted by Fig. 18 to the observed normalized averaged intensities given in Table 5 ($cf.$ Fig. 20 also). Since the L value for sample B is near to that for minimum loss in Fig. 18, it is simplest to compare the other samples to sample B. Sample A shows
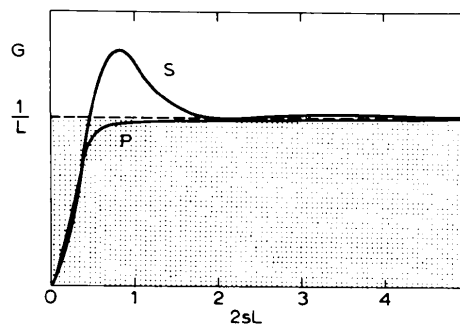

Fig. 21. Calculated values of G as a function of $2sL$. Curve S is for spherical particles and curve P for pyramidal particles. In each case the results are averaged over a range of particle sizes to remove oscillatory terms which are not observed in practice. The area under a curve may equal, but not exceed, the shaded area.
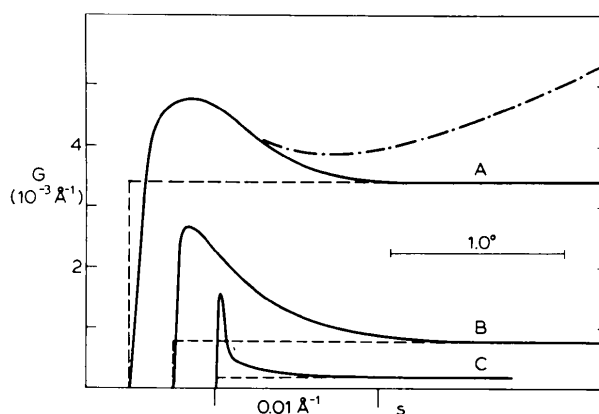

Fig. 22. The function G for the 200 reflection vs deviation from the Bragg condition, $s = (\cos \theta / \lambda) \Delta(2\theta)$, for three of the MgO samples studied. The dot–dash line shows the non-physical result obtained if the background found for sample C is used for interpretation of sample A. Although each curve has initial slope zero, the steep portion of each curve projects to very near the origin. The origins for the various curves are displaced by 0·25° for clarity. For an ideally mosaic sample, the area enclosed by each curve must be less than the area of the corresponding dashed rectangle.

a comparative loss close to what might be predicted. Sample C would be expected to show a large extinction loss. The loss for $L = 6000$ Å would be about 10 % for platelet particles and more for other particle shapes. (The small s thickness parameter, which would be important for determining extinction, is equal to L for platelet particles. It can be shown that the small s parameter can be larger, but not smaller, than this value.) In actual fact, the measurements on sample C were complicated by preferred orientation, but it was completely clear that sample C gave the largest integrated intensities and that there could not have been appreciable extinction.

A thorough discussion of this inconsistency would be beyond the scope of this review and perhaps beyond the present state of diffraction theory. But we should point out that the situation is that the scattering in the wings of the reflection is smaller than would be required by the mosaic model (thus giving rise to inappropriately large L values). We have also done experiments on the wings of reflections in mosaic single crystals, and here also the scattering is too small. These reductions no doubt arise from lack of complete independence of the individual crystallites required by the ideally mosaic model. That is, the crystallites are not separated by empty space but by non-crystalline material. It is perhaps because of this reduced scattering in the wings of the reflections that it appears to be possible to separate Bragg peaks more easily than the analysis of §3.1 would indicate.

3.2.4 Nearly amorphous scattering

Deviations from ideally mosaic behaviour can also be seen in the scattering very far from the Bragg peaks. As has been mentioned already, the 'backgrounds' were chosen separately for each sample studied. These backgrounds were appreciably different as indicated in Fig. 19 and implied by the dot–dashed curve in Fig. 22. The excess background for sample A, for example, with respect to sample C could be estimated with fair accuracy in the region from 2 to 10° away from Bragg peaks. This excess did not have a strong angular dependence. It thus seems appropriate to refer to it as nearly amorphous scattering. The amount of amorphous scattering was greater for samples having smaller particle sizes and presumably arose from atoms in the various imperfections that determine mosaic crystallite boundaries.

A quantitative measure of the amorphous scattering can be obtained from the information on Fig. 19 and a generalization of equations (2) and (6) to the case of two atoms per unit cell. We find that $a_{am} = 0.043 \times F^2/2\mu_0$, where F is the value appropriate to 200, the area of which is indicated by the rectangle in the figure. This value of a_{am} assumes a level of amorphous scattering given by the difference in intensity between the two arrows in Fig. 19. Although the amorphous intensity drops off at higher angles, in first approximation a_{am} can be considered to have a constant value throughout the 200 unit cell in reciprocal space. It is also the case that the integral of the scattering over a unit cell in reciprocal space is approximately conserved (LaFleur, 1969, 1970). Thus the above result could be described as a loss of 4·3 % of the Bragg scattering into amorphous scattering.

The results depicted in Fig. 15 indicate that a similar situation obtains for the nickel samples. Because of the ductility of nickel and the cold work introduced during the pelleting procedure, it was more difficult to carry out a complete line-shape analysis in this case. Because of this difficulty and because of possible uncertainties in the calculated values used to establish Fig. 15, we can only estimate a possible amorphous scattering of about 0·002 e.u. cm in this case. This

estimate was verified, in the angular range 30° to 85°, by comparing the scattering of pressed samples to that from a sample annealed at 600 °C. The excess could again be attributed to nearly amorphous scattering. It ranged from $\overline{a_{am}} = 0.0015$ for a sample pressed at 6 MPa to $\overline{a_{am}} = 0.0025$ for one pressed at 470 MPa, in agreement with the estimates based on the detailed accounting leading to Fig. 15. These values represent about 0·5 to 1 % of the $f^2/2\mu_0$ values appropriate to this angular range.

II.4. Conclusions

Based on our experience as reported in this paper and based on the results of the 1966–1969 Powder Project, we might indicate our opinion of the requirements, limitations and possibilities for the accurate measurement of structure factors from powders.

It is clear that an effort of some magnitude is required to achieve the highest accuracies. We should emphasize, however, that it is very little additional effort to obtain absolute values rather than accurate relative values. For the latter, for example, one needs to measure the polarization ratio, analyze peak shapes, determine the average wavelength, characterize the sample, etc. The addition of a foil container and the calibration of the foils is little additional work. Such foils are also a great help in comparing fluxes of appreciably different power.

Even assuming that accurate values of the Bragg scattering were available, the absolute analysis of § II.2 or the comparative analysis of § II.3 indicates that an error of 2–4 % in F might be expected from a straightforward application of equation (6) to the kinds of material being considered here. This error might be reduced somewhat by complex extrapolation of results obtained on a series of powders. (For example, extrapolate the background to that of a very well annealed sample and the peak area to that of a sample with unmeasurably broad peaks.) Such accuracies would require careful measurement of the absorption coefficient, a problem touched only lightly here. But, more fundamentally, it would require formulas and extrapolation techniques based on a true understanding of the diffraction from real samples (rather than the unrealizable, idealized sample of equation 6). It is not clear that such an understanding is possible at present.

There is the presumption that the participants in the Powder Project took more than routine care. Thus the discrepancies of more than 5 % must be counted as discouraging. Nevertheless, it is our opinion that the Bragg scattering from a given powder can be determined to better than 1 % in E_{hkl} if the precepts outlined here are carefully followed. This figure might be improved to about $\frac{1}{2}$ % if a given sample of the given powder is considered, as indicated in Table 4. These estimates of accuracy can most easily be refuted or verified through international cooperation, and we reiterate our invitation to obtain a duplicate of the standard sample (apply to P. Suortti).

References

ALBANESE, G. & GHEZZI, C. (1973). *Phys. Rev.* B**8**, 1315–1323.

BIRGENEAU, R. J., CORDES, J., DOLLING, G. & WOODS, A. D. B. (1964). *Phys. Rev.* **136**, A1359–A1365.

BOCKSTIEGEL, G. (1966). *Modern Developments in Powder Metallurgy.* Edited by H. H. HAUSNER, Vol. 1, pp. 155–186. New York: Plenum.

BORIE, B. (1961). *Acta Cryst.* **14**, 566–568.

BRADACZEK, H. & HOSEMANN, R. (1968). *Acta Cryst.* A**24**, 568–577.

CARDONA, M. (1974). *Elementary Excitations in Solids, Molecules and Atoms.* Edited by J. T. DEVREESE, A. B. KUNZ & T. C. COLLINS, Vol. *B*, pp. 269–291. London: Plenum.

CHIPMAN, D. R. (1969). *Acta Cryst.* A**25**, 209–214.

CHIPMAN, D. R. & PASKIN, A. (1959a). *J. Appl. Phys.* **30**, 1992–1997.

CHIPMAN, D. R. & PASKIN, A. (1959b). *J. Appl. Phys.* **30**, 1998–2001.

COCHRAN, W. (1963). *Rep. Prog. Phys.* **26**, 1–45.

CROMER, D. T. (1969). *J. Chem. Phys.* **50**, 4857–4859.

CURRAT, R., DeCICCO, P. D. & WEISS, R. J. (1971). *Phys. Rev.* B**4**, 4256–4261.

DeMARCO, J. J. & SUORTTI, P. (1971). *Phys. Rev.* B**4**, 1028–1033.

EISENBERGER, P. & PLATZMAN, P. M. (1970). *Phys. Rev.* A**2**, 415–423.

FREEMAN, A. J. (1959). *Acta Cryst.* **12**, 929–936.

GANGULEE, A. (1974). *J. Appl. Cryst.* **7**, 434–439.

GUINIER, A. (1963). *X-ray Diffraction.* San Francisco: W. H. Freeman.

HERVET, H. & OBER, R. (1973). *J. Phys. C,* **6**, 3024–3032.

International Tables for X-ray Crystallography (1974). Vol. IV. Birmingham: Kynoch Press.

JÄRVINEN, M., MERISALO, M., PESONEN, A. & INKINEN, O. (1970). *J. Appl. Cryst.* **3**, 313–318.

JENNINGS, L. D. (1968). *Acta Cryst.* A**24**, 472–474.

JENNINGS, L. D. (1969). *Acta Cryst.* A**25**, 217–222.

KEATING, D. T. & WARREN, B. E. (1952). *Rev. Sci. Instrum.* **23**, 519–522.

LAFLEUR, P. L. G. M. (1969). *Acta Cryst.* A**25**, 643–650.

LAFLEUR, P. L. G. M. (1970). *Acta Cryst.* A**26**, 674–678.

LINKOAHO, M., RANTAVUORI, E. & KORHONEN, U. (1971). *Acta Cryst.* A**27**, 495–496.

MATERLIK, G. (1975). Dissertation, Univ. Dortmund.

MILLER, G. G. S. & BLACK, P. J. (1970). *Acta Cryst.* A**26**, 527–532.

MITRA, G. B. & CHAUDHURI, A. K. (1974). *J. Appl. Cryst.* **7**, 350–355.

O'CONNOR, D. A. & BUTT, N. M. (1963). *Phys. Lett.* **7**, 233–235.

OLEKHNOVICH, N. M. (1969). *Sov. Phys. Crystallogr.* **14**, 203–206.

OLEKHNOVICH, N. M. (1970). *Sov. Phys. Crystallogr.* **14**, 724–727.

PAAKKARI, T. (1974). *Acta Cryst.* A**30**, 83–86.

PAAKKARI, T. & SUORTTI, P. (1974). *Phys. Rev.* B**9**, 1756–1761.

PAAKKARI, T., SUORTTI, P. & INKINEN, O. (1970). *Ann. Acad. Sci. Fenn.* A**VI**, No. 345, 1–29.

PASKIN, A. (1959). *Acta Cryst.* **10**, 667–669.

PAWLEY, G. S. (1969). *Acta Cryst.* A**25**, 702–707.

PESONEN, A., JÄRVINEN, M. & KURKI-SUONIO, K. (1973). *Phys. Fenn.* **8**, 81–91.

PIRIE, J. D., REID, J. S. & SMITH, T. (1971). *J. Phys. C,* **4**, 289–297.

PLATZMAN, P. M. (1974). *Elementary Exitations in Solids, Molecules and Atoms.* Edited by J. T. DEVREESE, A. B. KUNZ and T. C. COLLINS, Vol. *A*, pp. 31–64. London: Plenum.

PLATZMAN, P. M. & TZOAR, N. (1965). *Phys. Rev.* **139**, A410–A413.

RACHINGER, W. A. (1948). *J. Sci. Instrum.* **25**, 254–255.

SCHULZ, L. G. (1949). *J. Appl. Phys.* **20**, 1030–1033.

SPARKS, C. J. (1974). *Phys. Rev. Lett.* **33**, 262–265.

STEVENS, B. A. (1973). *Bell Lab. Rep.* No. 252.

SUORTTI, P. (1967). *Ann. Acad. Sci. Fenn.* A**VI**, No. 240, 1–33.

SUORTTI, P. (1972). *J. Appl. Cryst.* **5**, 325–331.

SUORTTI, P. (1974). *Phys. Fenn.* **9**, 49–56.

SUORTTI, P. (1975). *Phys. Fenn.* **10**, 161–166.

SUORTTI, P. (1977). Unpublished.

SUORTTI, P. & JENNINGS, L. D. (1971). *J. Appl. Cryst.* **4**, 37–43.

SUORTTI, P. & PAAKKARI, T. (1968). *J. Appl. Cryst.* **1**, 121–122.

WAGNER, C. N. J. (1966). *Local Atomic Arrangements studied by X-ray Diffraction.* Edited by J. B. COHEN and J. E. HILLIARD, pp. 219–268. New York: Gordon and Breach.

WALKER, C. B. (1956). *Phys. Rev.* **103**, 558–561.

WALKER, C. B. & CHIPMAN, D. R. (1972). *Acta Cryst.* A**28**, 572–580.

WALLER, I. & HARTREE, D. R. (1929). *Proc. Roy. Soc.* A**124**, 119–142.

WARREN, B. E. (1969). *X-ray Diffraction.* Reading, Mass.: Addison-Wesley.

WEINBERG, D. L. (1964). *Phys. Rev.* **134**, A1016–A1018.

WILSON, A. J. C. (1962). *X-ray Optics.* London: Methuen.

WILSON, A. J. C. (1963). *Mathematical Theory of X-ray Powder Diffractometry.* Eindhoven: Centrex.

ZACHARIASEN, W. H. (1945). *Theory of X-ray Diffraction in Crystals.* New York: John Wiley.